

Supplementary Information:

Microporous Transport Layers Facilitating Low Iridium Loadings in Polymer Electrolyte Water Electrolysis

Carl Cesar Weber ^a, Salvatore De Angelis ^{a,b}, Robin Meinert ^a, Christian Appel ^c, Mirko Holler ^c, Manuel Guizar-Sicairos ^{c,d}, Lorenz Gubler ^a, Felix N. Büchi ^{a,*}

^aElectrochemistry Laboratory, Paul Scherrer Institut, 5232 Villigen PSI, Switzerland

^bPresent address: Technical University of Denmark, 2800 Kgs. Lyngby, Denmark

^cPhoton Science Division, Paul Scherrer Institut, 5232 Villigen PSI, Switzerland

^dInstitute of Physics (IPHYS), Ecole Polytechnique Fédérale de Lausanne, Rte Cantonale, Lausanne 1015, Switzerland

*Corresponding author: felix.buechi@psi.ch

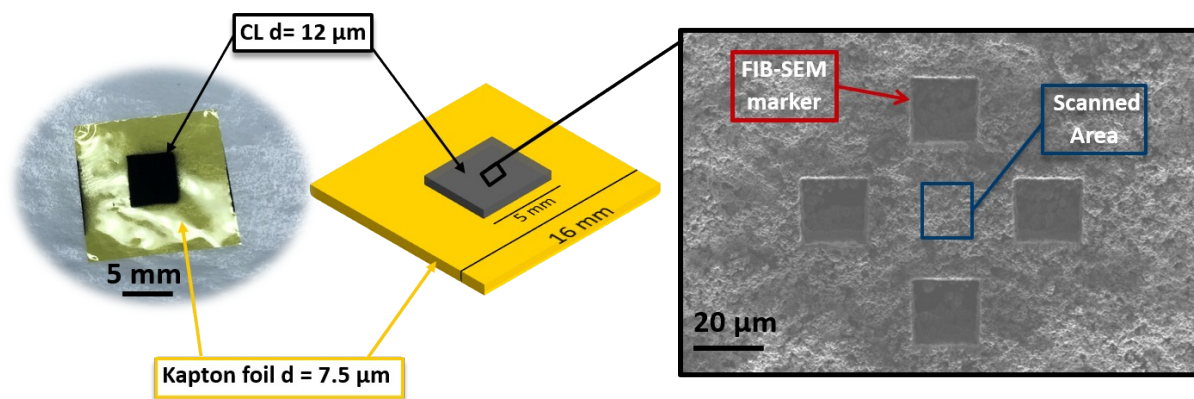


Figure S1 Scheme illustrating the catalyst layer samples scanned by PyXL and the FIB-SEM markers used to identify the identical location.

Figure S1 shows a schematic illustration and a picture of the catalyst layer (CL) sample that was used for Ptychographic X-ray Laminography (PyXL). The CL with an area of $5 \times 5 \text{ mm}^2$ was spray-coated on a thin Kapton foil (thickness $d = 7.5 \text{ μm}$). To identify the identical location in dry and wet states, FIB-SEM drilled markers ($20 \times 20 \text{ μm}$) were placed around the planned scanning area.

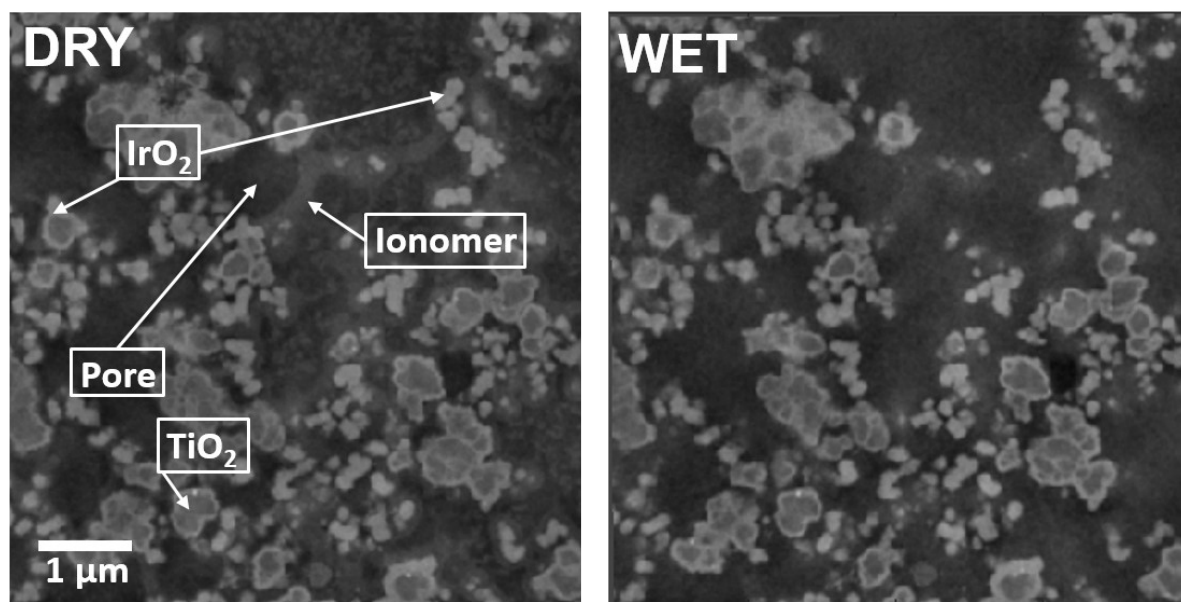


Figure S2. 2D slices out of the 3D volume of the anodic catalyst layer obtained by PyXL in dry and wet comparison.

In Figure S2 the 2D slices obtained from the PyXL 3D volume of the anodic catalyst layer (CL) are shown for the dry and wet state. We can observe that the dry phases (IrO_2 and TiO_2) are relatively stable and can be distinguished precisely in both the dry and wet states. The pore and ionomer phase is also distinguishable in the dry state and can be segmented similarly to previous reports using ptychographic X-ray computed tomography (PXCT).^[1] In the wetted state on the contrary, the contrast between the wet ionomer and the pores, now filled with liquid water, is poor due to a decreased difference in electron and mass density between water/wet ionomer ($\sim 0.6 \text{ g cm}^{-3}$) compared to air/dry ionomer (2.1 g cm^{-3}).

Therefore, the segmentation of these two phases is not reliable even when using Fiji's trainable WEKA segmentation tool.

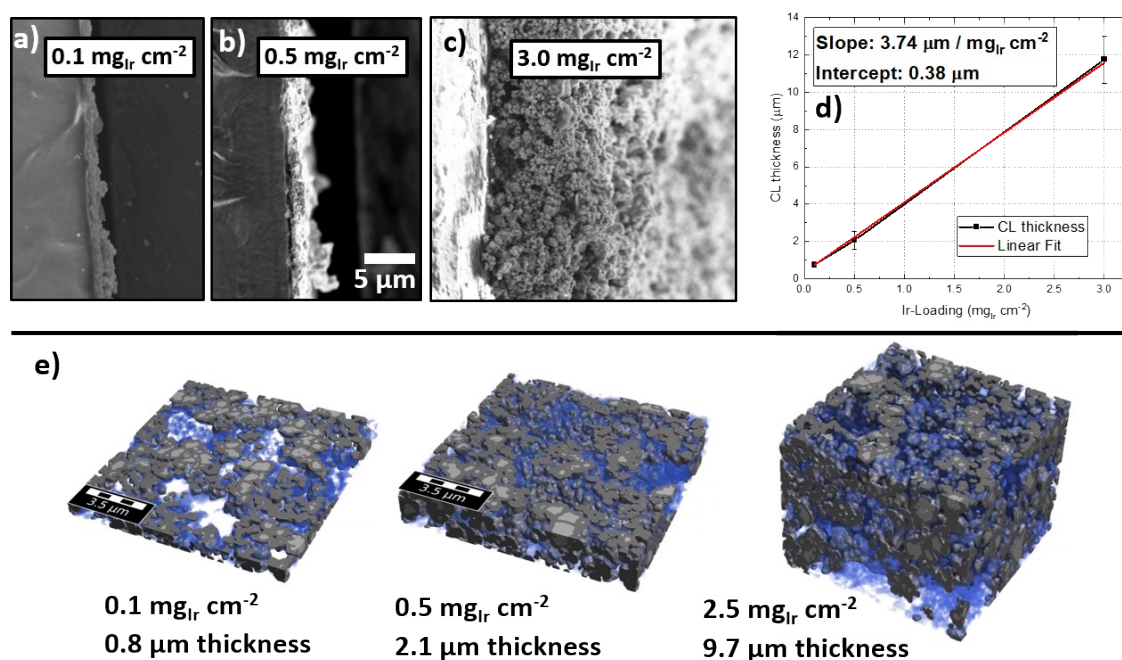


Figure S3. Crosssection SEM of the anodic side of the CCM at three loadings of a) low loading of $0.1 \text{ mg}_{\text{Ir}} \text{ cm}^{-2}$ b) medium loading of $0.5 \text{ mg}_{\text{Ir}} \text{ cm}^{-2}$ and c) higher loading of $3.0 \text{ mg}_{\text{Ir}} \text{ cm}^{-2}$. d) Linear correlation of measured CL thickness and respective Iridi, loading. e) Surface renderings of the cropped 3D volume of the CL (PyXL) at the respective loadings investigated in the electrochemistry part.

The SEM cross-sections of the anodic CL shown in Figure S3a-c were obtained by freezing and cracking the different CL coated on the Nafion membrane. From the images, the average thickness was estimated and correlated to the loading where a linear correlation was obtained as seen in Figure S3d. From the obtained thicknesses, the 3D volumes from PyXL were cropped to the respective thickness of the loading of interest, which were used to compute and compare the CL electronic conductivity.

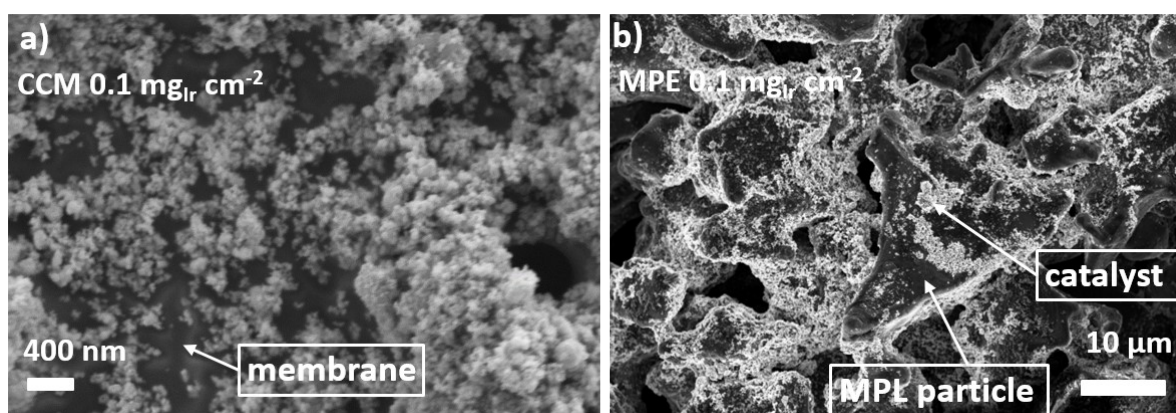


Figure S4. SEM image of the anodic catalyst layers with low loading of $0.1 \text{ mg}_{\text{Ir}} \text{ cm}^{-2}$ a) in a catalyst-coated membrane (CCM) configuration and b) in a microporous electrode (MPE) configuration.

Figure S4 exhibits top-view SEM images of the catalyst layers at low Ir loading ($0.1 \text{ mg}_{\text{Ir}} \text{ cm}^{-2}$) in both configurations. Figure S4a) shows the CL in a catalyst-coated membrane (CCM). The interruptions in the percolation network are clearly visible since parts of the membrane (black) are not coated by the catalyst. Figure S4b) shows the respective microporous electrode (MPE) approach at equal loading. We can observe how the microporous layers (MPL) particles are only partially covered by the catalyst, leading to severe interruptions in the percolation network.

Table S1. Transport properties of the MPL and the support layer (SL) in all spatial directions were obtained from XTM analysis. IP: in-plane, TP: through-plane.

Layer	Spatial Direction	Tortuosity (pore)	Rel. Diffusivity (%)	Abs. Permeability ($\times 10^{-12} \text{ m}^2$)	Thermal conductivity (W/(mK))	Electrical conductivity ($\times 10^6 \text{ S/cm}$)
MPL	X (IP)	2.0	25	1.2	5.1	0.54
	Y (IP)	2.0	25	1.3	5.1	0.55
	Z (TP)	2.5	20	0.96	4.0	0.46
SL	X (IP)	3.2	8.7	7.3	10.4	1.1
	Y (IP)	3.1	8.7	8.0	10.4	1.1
	Z (TP)	3.0	9.1	8.2	10.1	1.1

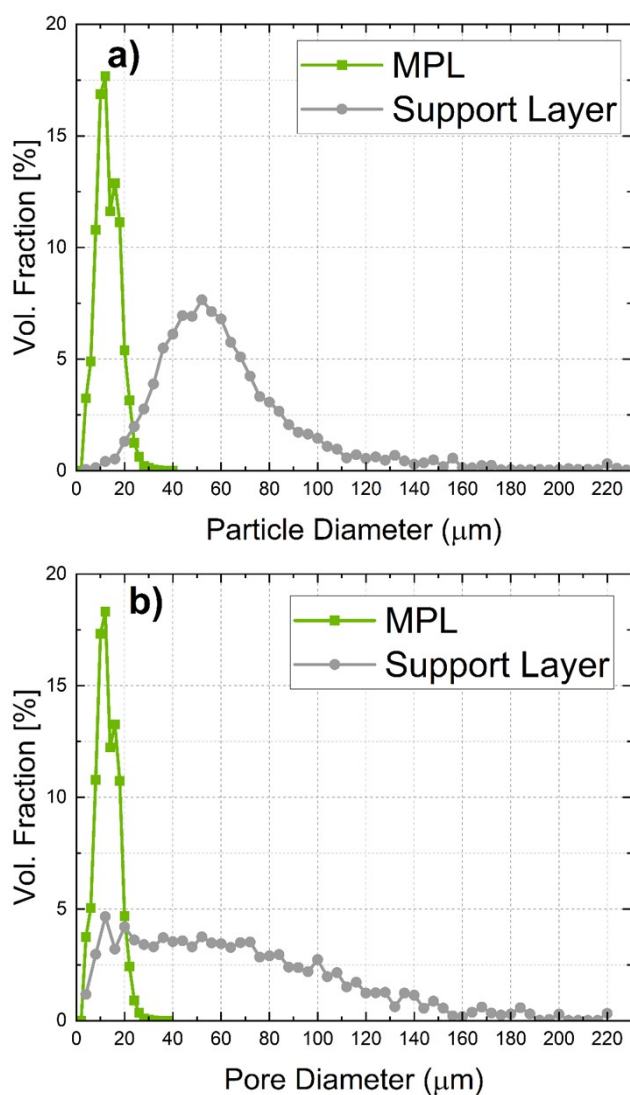


Figure S5. a) Particle and b) pore size distribution of the MPL and its respective support layer.

In

Figure S4 exhibits top-view SEM images of the catalyst layers at low Ir loading ($0.1 \text{ mg}_{\text{Ir}} \text{ cm}^{-2}$) in both configurations. Figure S4a) shows the CL in a catalyst-coated membrane (CCM). The interruptions in the percolation network are clearly visible since parts of the membrane (black) are not coated by the catalyst. Figure S4b) shows the respective microporous electrode (MPE) approach at equal loading. We can observe how the microporous layers (MPL) particles are only partially covered by the catalyst, leading to severe interruptions in the percolation network.

Table S1 the transport properties of the MPL and support layer (SL) that were obtained from the X-ray tomographic microscopy (XTM) data are given. The values are similar to previous reports of MPLs in

the literature.^[2] We can observe that the absolute permeability of the MPL is lower than for the SL, but still roughly three orders of magnitude higher than for the CL structure. The electrical conductivity of the MPL is slightly lower than for the SL but in both cases still roughly six orders of magnitude higher than the conductivity of the CL. Figure S5a shows the particle size distribution and Figure S5b the pore size distribution of the MPL and SL. The size distribution of the MPL is drastically narrower, peaking on the lower end of the scale at roughly 10 – 15 μm , both in the particle and pore size.

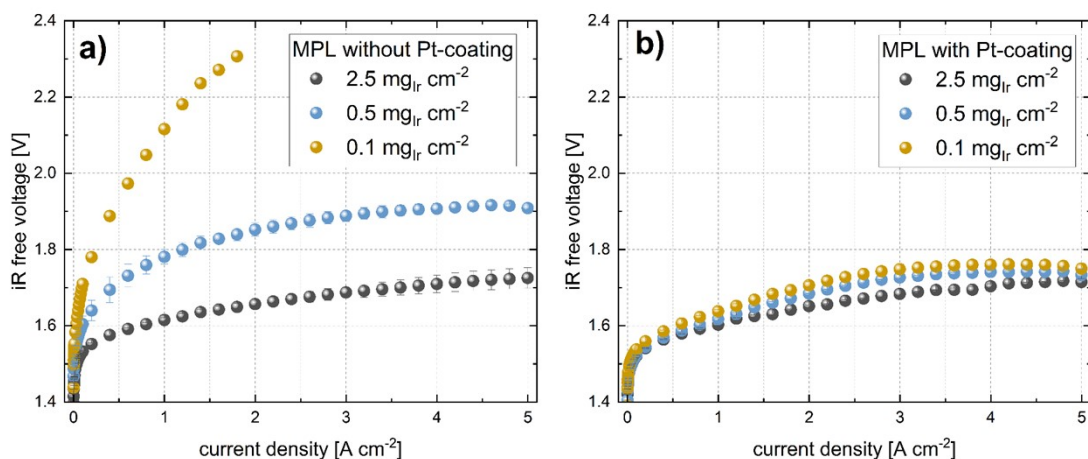


Figure S6. *iR*-free polarization curves of all loadings in CCM configuration using a) MPL without Pt-coating and b) MPL with Pt-coating.

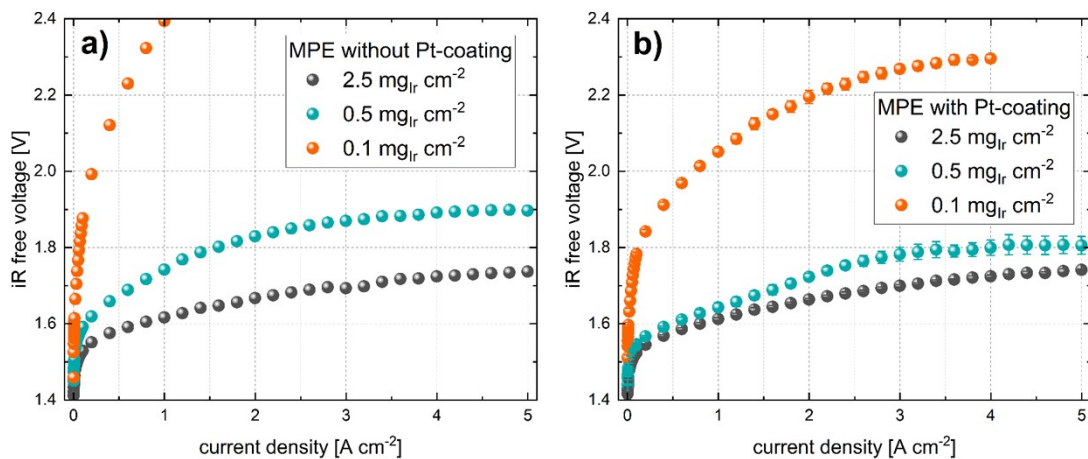


Figure S7. *iR*-free polarization curves of all loadings in MPE configuration using a) MPL without Pt-coating and b) MPL with Pt-coating.

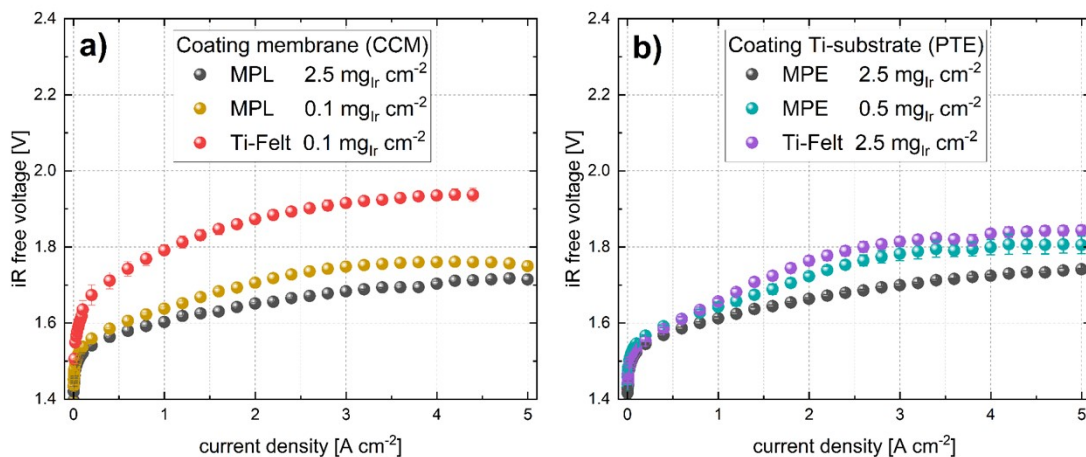


Figure S8. *iR*-free polarization curves of selected MPL measurements benchmarking them to measurement using single-layer Ti-felt in a) CCM b) MPE configuration, in all cases using equal Pt-coating procedure on the MPL/PTL.

Figure S6, Figure S7, and Figure S8 show the *iR*-free polarization curves of all performance measurements reported in the manuscript. When Pt coatings are used on the MPL, the differences are relatively low, indicating that most differences can be attributed to the high-frequency resistance measurement. For the measurements without Pt-coating, we still observe significant differences in *iR*-free cell voltage, indicating that a considerable contribution is still related to the kinetic overpotentials as can be seen in kinetic analysis in section 2.4 of the manuscript. At high current density, a slight drop in the potential can be observed. This could be caused by a localized increase in temperature that occurs at high current densities. This temperature increase may not only affect the measured HFR (as previously shown^[3-5]) but also the OER kinetics. This, in turn, could explain the observed drop in potential for the highest current densities.

Literature

- [1] S. De Angelis, T. Schuler, M. Sabharwal, M. Holler, M. Guizar-Sicairos, E. Müller, F. N. Büchi, *Sci Rep* **2023**, *13*, 4280.
- [2] T. Schuler, J. M. Ciccone, B. Krentscher, F. Marone, C. Peter, T. J. Schmidt, F. N. Büchi, *Adv. Energy Mater.* **2020**, *10*, 1903216.
- [3] M. Suermann, T. J. Schmidt, F. N. Büchi, *Electrochimica Acta* **2016**, *211*, 989.
- [4] T. Schuler, T. J. Schmidt, F. N. Büchi, *J. Electrochem. Soc.* **2019**, *166*, F555.
- [5] C. C. Weber, T. Schuler, R. De Bruycker, L. Gubler, F. N. Büchi, S. De Angelis, *Journal of Power Sources Advances* **2022**, *15*, 100095.